

Effects of Potassium Treatment on SnO₂ Electron Transport Layers for Improvements of Perovskite Solar Cells

SeongYeon Kim,^{a,b,†} Fei Zhang,^b Jinhui Tong,^b Xihan Chen,^b Enkhjargal Enkhbayar,^a Kai Zhu,^b JunHo Kim^{a,*}

^aDepartment of Physics, Incheon National University, Incheon 22012, Republic of Korea

^bChemistry and Nanoscience Center, National Renewable Energy Laboratory, Golden, CO 80401, United States of America

[†]Current Affiliation : Research Center for Thin Film Solar Cells, Daegu Gyeongbuk Institute of Science and Technology (DGIST), Daegu 42988, Republic of Korea

*Corresponding Author: JunHo Kim(jhk@inu.ac.kr)

Abstract

SnO₂ has been studied intensively as an electron transport layer (ETL) for highly efficient metal halide perovskite solar cells. However, SnO₂ ETL frequently exhibits defect-related issues associated with the bulk SnO₂ and the perovskite/SnO₂ interface, and to passivate the defect states potassium ion has been used. In order to investigate the passivation effect of potassium ion, we carried out KCl treatment on the solution-processed SnO₂ ETL. The K⁺ ion was observed to diffuse into the perovskite absorber, causing a reduction of the band gap of perovskite absorber with possible upshift of the conduction band minimum and a better conduction band alignment. Admittance spectroscopy revealed that diffused K⁺ ions can passivate defects of the perovskite absorber layer. With the KCl treatment, the J-V hysteresis was almost eliminated, and power conversion efficiency was much enhanced with improved open-circuit voltage and fill factor.

Keywords: SnO₂, perovskite, solar cell, defect passivation, K treatment, electron transport layer

1. Introduction

Organic–inorganic metal halide perovskite solar cells (PSCs) have recently reached power conversion efficiency (PCE) of more than ~25%, which is the highest among polycrystalline thin-film solar cells.¹ For high-efficiency PSCs, an n-i-p device architecture with mesoporous titanium dioxide (TiO₂) is widely used as an electron transport layer (ETL) owing to its wide band gap energy, high electron affinity, and good mobility.²⁻⁴ However, a high temperature (> 450 °C) is often required for TiO₂ processing. The high-temperature process hinders the application of TiO₂-employed PSCs to tandem cell structures and flexible solar cells on a polymer or plastic substrates. To address this challenge, SnO₂ has recently attracted significant attention as a promising alternative material for the ETL. SnO₂ films can be processed at a relatively low temperature (< 200 °C) using several techniques, such as spin coating of nanoparticles,^{5,6} spin coating of thin films,^{7,8} chemical bath deposition,⁹ atomic layer deposition^{10,11} and slot-die printing,¹² and sputtering methods.¹³ Moreover, SnO₂ exhibits good optical and electrical properties. In particular, it features a wide band gap energy (3.6–4.0 eV) and low conduction band minimum (CBM), providing good conduction band alignment with perovskite absorbers, which ultimately results in stable and high-efficiency solar cells.^{4,6,7,9,10,12-16}

However, low-temperature solution-processed SnO₂ could suffer from surface imperfections compared to high-temperature processed TiO₂. This decreases the PCE and cell stability. Solution-processed SnO₂ is generally known to have hydroxyl groups, which generate defect states in the valence band¹⁷ and impair band alignment between the perovskite absorber and SnO₂ ETL.¹⁸ To passivate the surface defects of SnO₂, various methods (post-UV-ozone treatment,¹⁹ fullerene-derivative treatment,²⁰ NdCl₃ treatment,²¹ PCBM treatment,^{22,23} EDTA-SnO₂,²⁴ NH₄F treatment²⁵, and potassium treatment^{12,26-30}) have been proposed. Potassium treatment with KCl is very effective for a simple device fabrication. Zhu et al. reported that KCl treatment passivated interface defects both at ETL/perovskite interface and at the grain boundary of a perovskite absorber, which increased solar cell stability and PCE.²⁷ Wang et al. concluded that K⁺ and Cl⁻ diffused into perovskite bulk, improving perovskite crystallinity and

passivating the defect by inserting KCl into the ETL/perovskite interface.²⁸ It was also reported that the inserted KCl shifted a conduction edge higher, thus, increasing both V_{oc} and PCE.³⁰ Liu et al also showed that the KCl treatment mainly improved the ETL/perovskite interface rather than the perovskite bulk by providing both TEM-EDS and SIMS results.²⁶ As seen, the various potassium effects were empirically proven using the lab-to-lab experiments. Moreover, to our knowledge, direct evidence of the suppression of bulk defects by KCl treatment has not been demonstrated.

In this study, we carried out KCl treatment on a SnO_2 ETL and examined the corresponding effect on device performance. We found KCl treatment modifies the band gap and suppresses defects of the perovskite absorber, which significantly suppresses the hysteresis in the current density voltage (J-V) curve and enhances the PCE. The improved properties of KCl treatment are verified with various characterizations including photoluminescence (PL), time-resolved photoluminescence (TRPL), admittance spectroscopy (AS), and electrochemical impedance spectroscopy (EIS).

2. Experimental Procedures

Materials

Tin(IV) chloride pentahydrate ($\text{SnCl}_4 \cdot 5\text{H}_2\text{O}$), tin(II) chloride dihydrate ($\text{SnCl}_2 \cdot 2\text{H}_2\text{O}$), urea, thioglycolic acid, hydrochloric acid (37% wt.) Methylamine hydrochloride (MACl), N,N, dimethyl formamide (DMF), dimethyl sulfoxide (DMSO), 4-tert-butylpyridine (TBP), Li-TFSI, and potassium chloride (KCl) were purchased from Sigma-Aldrich. Methylammonium bromide (MABr), PbBr_2 , and PbI_2 were purchased from TCI. Formamidinium iodide (FAI) and Co(III)-TFSI (FK102) were purchased from Dyesol. Spiro-OMeTAD(LT-S922) was purchased from Lumtec.

Device Fabrication

Initially, we sonicated the ITO-coated glasses with acetone for 15 min, isopropyl

alcohol for 15 min, and DI water for 15 min. Before coating the SnO₂ film, UV-ozone treatment was performed for 15 min on a precleaned substrate. To prepare the solution for SnO₂ spin coating, we dissolved 0.05 M of SnCl₄·5H₂O in isopropyl alcohol (IPA). Using a micropipette, 200 µl of the solution was dropped onto the substrate and spun at 3000 rpm for 30 s, followed by predrying at 100 °C for 10 min and then air annealing at 180 °C for 1 h. After the spin-coating process, the samples were treated with UV-ozone again for 15 min.

After spin coating, the SnO₂ layer was coated via chemical bath deposition (CBD).⁹ To prepare the CBD solution, we dissolved 0.002 M of SnCl₂·2H₂O in 720 ml of deionized water, adding 1.5 g of urea, 30 µl of thioglycolic acid, and 1.5 ml of HCl (37 wt %), followed by stirring for 2 min. Then, we inserted the substrates vertically into the CBD solution and maintained them at 70–80 °C for 3 h. The temperature was carefully controlled using a hot water jacket, and the water in the outer jacket was stirred using a magnetic bar to obtain a uniform temperature. The CBD-processed substrates were rinsed with deionized water for 2 min in a sonication bath to remove precipitated particles and then air annealed at 180 °C for 1 h. The substrates were then subjected to UV-ozone treatment for 15 min.

After deposition of the SnO₂ ETL, KCl treatment was conducted. KCl solutions were prepared by dissolving KCl concentrations of 5, 8, 13, and 18 mg/ml in DI water. We dropped 200 µl of the KCl solution on the substrates and spun them at 5000 rpm for 60 s. Then, the substrates were predried at 100 °C for 10 min and then air annealed at 200 °C for 1 h. Afterward, we again performed UV-ozone treatment on the substrates for 15 min.

For the (FAPbI₃)_{0.92}(MAPbI₃)_{0.08} perovskite solvents, 1.6 ml of DMF and 0.4 ml of DMSO were mixed. In that solvent, 1.4 M of FAI, 1.53 M of PbI₂, 0.11 M of MABr, 0.12 M of PbBr₂ and 0.5 M of MACl were dissolved. We also prepared a solution of hole transport material by dissolving 0.2102 g of Spiro-OMeTAD, 82 µl of TBP, 48.35 µl of Li-TFSI (1.8 M in acetonitrile) and Co-TFSI (0.25 M in acetonitrile) into 2.3 ml of chlorobenzene. The perovskite and spiro-OMeTAD solutions were stirred using a vortex machine for 3 h.

Perovskite films were spin-coated by dropping 120 µl of perovskite solution at 1000 rpm for 10 s and 5000 rpm for 30 s under nitrogen ambient. Then, 1 ml of the antisolvent

diethyl ether was quickly dropped onto the spinning substrate at 20 s before spin-coating was completed. Then, we annealed the spin-coated perovskite films at 150 °C for 10 min. The hole transport layer (HTL) of spiro-OMeTAD was spin-coated by dropping 70 μl of the HTL solution at 4500 rpm for 25 s without post annealing.

To complete the device structure, 120 nm thick Ag was deposited as a grid pattern by thermal evaporation. Before thermal evaporation, the base pressure of the vacuum chamber was reduced to 8×10^{-7} Torr. The deposition rate of Ag was maintained at 0.5 $\text{\AA}/\text{s}$ for the first 10 nm and then 2 $\text{\AA}/\text{s}$ for the rest of the deposition.

Characterization of materials and devices

XRD. The crystal structures of the perovskite films were characterized using an X-ray diffractometer (XRD, D-Max 2200, Rigaku). The operation was conducted in theta/2theta scan mode with Cu K α radiation at 40 kV and 250 mA.

SEM. The surface morphology of the perovskite absorbers was examined via field-emission scanning electron microscopy (FE-SEM) (Nova 630, FEI) with an electron beam voltage of 3 kV in the immersion-lens mode.

PL, TRPL, PL mapping, and UV-Vis spectroscopy. PL and TRPL data were acquired using an optically triggered streak camera system (C5410, Hamamatsu). All samples were photoexcited using a 517 nm laser at a 200 V voltage and 240 $\text{nm}\cdot\text{min}^{-1}$ scan speed. A Raman measurement system (UniRaman, Uninanotech) was used for PL mapping of perovskite absorbers ($10 \times 10 \mu\text{m}^2$) in sample scanning mode with a step distance of 0.5 μm . For the PL mapping, a 633 nm laser was used for the excitation laser, and a 100 \times objective lens was utilized to focus the laser beam. The optical absorption spectra of the perovskite films were measured using an ultraviolet-visible (UV-Vis) spectrophotometer (Cary-6000i, Agilent).

J-V and EQE measurements J-V curves were measured under AM 1.5G illumination (100mW cm^2 , Oriel Sol3A Class AAA Solar Simulator, Newport) and under nitrogen ambient in a glove box using a Keithley 2450 source meter with 10 mV steps and 10 ms delay time. The AM 1.5G illumination was calibrated using a standard Si solar cell (Oriel, VLSI standards)

and a KG2 filter. The active area of the perovskite solar cells was 0.058 cm² (determined by the metallic aperture). The external quantum efficiency (EQE) spectra of the devices were measured using a solar cell quantum efficiency measurement system (Mcsience).

EIS EIS was performed using an impedance spectroscopy measurement system (FRA32M with ECI10M add-on for high-frequency measurement, PGSTAT 302N, Autolab). The frequency range was from 1 MHz to 100 mHz with 10 frequencies per decade and 0.02 V of root-mean-square amplitude. During the measurement, the device was irradiated with AM 1.5G illumination.

AS To characterize the defect states of the perovskite solar cells, AS measurements were performed using an LCR meter (E4980A, Agilent). For the AS measurement, the applied AC voltage was 30 mV and AC frequency was applied to the solar cell from 100 Hz to 2 MHz at measurement temperatures of 300–180 K.

3. Results and Discussion

We investigated the crystalline characteristics of the fabricated perovskite films, which were deposited as ITO/SnO₂/KCl (0 mg/ml, 5 mg/ml, 13 mg/ml, 18 mg/ml, spin coating)/perovskite, via XRD. We refer to these films as KCl-0, KCl-5, KCl-13, and KCl-18 absorbers. **Fig. 1** shows the XRD patterns of the fabricated perovskite films, where KCl-untreated perovskite film (KCl-0 absorber) and the other KCl-treated perovskite films (KCl-5, KCl-8, KCl-13, and KCl-18 absorbers) were grown with a cubic structure. However, as the KCl concentration was increased, the (002) peak position was shifted to a lower Bragg angle, as shown in Fig. 1 (b). This implies that the lattice parameters are increased by the KCl treatment with a higher concentration of KCl. Tang et al. showed that as more K⁺ ions were doped into the perovskite film (FA_{0.85}MA_{0.15})_{1-x}Pb(I_{0.85}Br_{0.15})₃ (x = 0 to 0.2), the lattice parameter of the cubic structure was increased.³⁰ The XRD result of Fig. 1(c) also demonstrates the increase in lattice parameters with an increase in the KCl concentration. The increased lattice parameters, shown in Fig. 1(c), can potentially stem from the K⁺ ion doping from the KCl treatment. We discuss this aspect below while describing the results of the SIMS depth

profiles analysis. All XRD patterns exhibit PbI_2 (001) peaks, indicating that PbI_2 is in the segregated phase in all films. FE-SEM measurements also confirm the hypothesis regarding the segregated PbI_2 phase. **Fig. 2** shows the surface FE-SEM images of the KCl-0 and KCl-13 absorbers. The white area (due to the PbI_2 segregation) is observed at both absorbers and is more pronounced in the KCl-treated absorber. The occurrence of PbI_2 can be explained by the perovskite decomposition during heat treatment, and the PbI_2 increase is driven by the increased KCl concentration, as previously reported.²⁵ We examined cross-sectional structures for both KCl-0 and KCl-13 cells. Fig. S1 shows FE-SEM cross-sectional images of KCl-0 and KCl-13 cells, where no white phase of PbI_2 was observed. The cross-section images for both cells exhibited similar structures, showing no clear discrete grained structure.

To study the distribution of K^+ and Cl^- , KCl-0 and KCl-13 absorbers were analyzed using the SIMS depth profiling. **Fig. 3** shows the SIMS profiles of the KCl-0 and KCl-13 absorbers. An increased K^+ concentration is evidenced in the bulk of the KCl-13 absorber, suggesting that K^+ ions are diffused into the perovskite film. However, the K^+ cation intensity for the KCl-0 film was relatively low and close to the background level, as shown in Fig. 3(a). In contrast to the K^+ ion, Figs. 3(c) and 3(d) show similar Cl^- ion distributions for both absorbers. KCl-13 shows a slightly enhanced Cl^- ion intensity on the front side of the absorber. The existence of Cl^- ions in the bulk KCl-0 absorber is attributed to the spin-coated SnO_2 film. For the spin coating of SnO_2 , we used tin chloride, which remained after spin coating and diffused into the perovskite absorber during the annealing process of the spin-coated perovskite film. The SIMS measurements revealed that K^+ cations diffused and doped into the perovskite absorber. This result supports the increase in the crystal lattice, as indicated by the XRD results in Fig. 1.

We also examined the optical properties of the KCl-untreated and KCl-treated perovskite absorbers. **Fig. 4** shows the PL, TRPL, and optical absorption measurements. From the comparison of the PL results (see Fig. 4(a)), the KCl-13 absorber shows a peak position at a longer wavelength (compared to the KCl-0 absorber), implying a decrease in the band gap of the KCl-13 absorber. The PL intensity and TRPL lifetime are usually correlated. When the

photoabsorber shows a higher (lower) PL intensity, it exhibits a longer (shorter) TRPL lifetime. Notably, PL intensity or TRPL lifetime can be affected by the following: (A) how fast photoelectrons sink into the ETL layer (photoelectron sink effect)^{14,15,20} and (B) how many defects are in the perovskite absorber or at the perovskite absorber/ETL interface, which act as charge recombination centers (the charge recombination effect).^{5,8,12,26} If effect (A) is dominant, the PL intensity is lower and the TRPL lifetime is shorter for the solar cell with better conduction band alignment at the absorber/ETL. If effect (B) is dominant, the PL intensity is higher and TRPL lifetime is longer for the solar cell with a lower density of recombination centers in the bulk absorber or at the absorber/ETL interface. For the PL and TRPL results, the two effects should be considered together. This is crucial because the KCl-0 absorber, with a higher deep defect density, exhibits much lower PCE. Figs. 4(a) and 4(b) show similar PL intensity and TRPL lifetime, where to be more precise KCl-13 shows a slightly higher PL intensity and a slightly longer TRPL lifetime (270 ns for KCl-13, 250 ns for KCl-0). If only the improved electron transfer at the absorber/ETL is considered (photoelectron sink effect), the KCl-13 absorber can potentially exhibit a lower PL intensity and shorter TRPL lifetime, which is not consistent with our results. We emphasize that the charge recombination effect should be considered as well for better understanding of our results. The charge recombination effect is observed when an absorber with a higher density of charge recombination centers shows a lower PL intensity and shorter TRPL lifetime. If we assume competition between the electron sink effect (A) and the charge recombination effect (B), the dominant effect will then determine the PL intensity and TRPL lifetime. Although the difference in PL intensity and TRPL lifetime is not significant in our study, a smaller PL intensity and TRPL lifetime for the KCl-0 absorber indicates that the charge recombination effect is a slightly more dominant factor than the electron sink effect. The defect level and defect density are discussed later in this paper. The perovskite absorbers of KCl-0 and KCl-13 were examined via PL mapping, as shown in Fig. S2 ($10 \times 10 \mu\text{m}^2$). PL mappings for FWHM, peak intensity, and wavelength of the peak position are displayed for both absorbers. We found that the FWHM of the KCl-13 absorber was smaller than that of the KCl-0 absorber, suggesting that the KCl-13 absorber has better crystallinity.

The peak intensity mapping (Fig. S2(c) and S2(d)) shows that the overall peak intensity is higher for the KCl-13 absorber than for the KCl-0 absorber, consistent with the result from Fig. 4(a). Mapping the wavelength of the peak position is not uniform here. The results from Fig. S2(e) and Fig. S2(f) are similar, but the KCl-13 absorber has a more uniform distribution and a smaller fraction of areas that exhibits a lower wavelength for the PL peak position. To check the band gap change caused by the K⁺ doping, optical absorption measurements were performed for both KCl-0 and KCl-13 absorbers. Figs. 4(c) and 4(d) show the optical absorption measurement results and the extracted optical band gaps, respectively. The optical band gaps of KCl-0 and KCl-13 are 1.59 eV and 1.58 eV, respectively, which is consistent with the PL results showing a decrease in band gap resulting from the K⁺ doping. According to Tang et al.,³⁰ as K⁺ ions are doped into perovskite absorbers, the band gap decreases with an upshift of the conduction band minimum (CBM). As our results also show K⁺ diffusion into the perovskite absorber (Fig. 3) and a decrease in the band gap for the KCl treated absorber (Fig. 4), the decrease in the band gap for the KCl-13 absorber is ascribed to K⁺ doping into the absorber by the KCl treatment.

We fabricated planar-type solar cells as in the structure of ITO/SnO₂/KCl (0 mg/ml, 5 mg/ml, 8 mg/ml, 13 mg/ml, 18 mg/ml)/perovskite/Spiro-OMeTAD/Ag (Fig. 5(a)) and compared the device properties. We refer to these devices as KCl-0, KCl-5, KCl-8, KCl-13, and KCl-18 cells, respectively. The fill factor (FF) and open circuit voltage (V_{oc}) increased with an increasing KCl concentration in the KCl treatment, which contributed to the increase in PCE. Moreover, we observed another trend that the hysteresis in the J-V curve is decreased with KCl treatment (Fig. 5(b)). The inset of Fig. 5(b) shows typical J-V curves for the KCl-untreated cell (device #4 of KCl-0 cell) and the KCl-treated cell (device #2 of KCl-13 cell) in Table S1–S4, where huge hysteresis is observed in KCl-0 cells and is significantly decreased in KCl-13 cells. If the hysteresis factor is defined as $(PCE_{\text{reverse}} - PCE_{\text{forward}}) / PCE_{\text{reverse}}$, it exhibits a decreasing trend, as shown in Fig. 5(b). The origin of the hysteresis has been explained in terms of (1) trap states from bulk or surface defects of perovskite, (2) polarization from ferroelectricity of perovskite, (3) ion migration of excess ions from interstitial defects.³² Furthermore, the hysteric

behavior due to ion migration can vary depending on the composition of the perovskite absorber (MA-containing perovskite with lower activation shows stronger hysteresis than FA-containing perovskite).³² As our absorber is a double cation (FA,MA)Pb(I,Br)₃ system, it is comparable to that reported by Tang et al., and hysteresis is eliminated by good conduction band alignment between the perovskite absorber and the ETL layer (TiO₂), caused by the upshift of the CBM of the perovskite absorber induced by the incorporation of K⁺ into the absorber layer. This can presumably explain the driver in our case, although we used SnO₂ as the ETL, which has a lower CBM than TiO₂. Defect passivation of the perovskite absorber by K⁺ incorporation also eliminates hysteresis. As we further explain in the description of Fig. 9, the defect level and defect density are significantly reduced in the KCl-treated perovskite. Hysteresis can be generated by ion migration related to the defect states in the perovskite. Lee et al. noted that K⁺ incorporation suppresses the iodine-related Frenkel defect and diminishes J-V hysteresis.³³ In our case, both the CBM upshift of the perovskite absorber and passivation of deep defects of the perovskite absorber are seemingly responsible for the suppression of the hysteresis. Further, the kink in the J-V curve of the KCl-0 solar cell is noteworthy. A kinked J-V curve is frequently observed when the conduction band is not well aligned between the absorber and the ETL, and it acts as a barrier layer for electrons. As normal SnO₂ usually has a lower CBM, the kink was rather unexpected in the J-V curve of the KCl-0 cell. However, according to the kinked J-V curve, CBM alignment between KCl-0 perovskite and SnO₂ was not very good, acting rather as an energy barrier. KCl treatment removed the J-V kink for the KCl-13 solar cell, causing the perovskite CBM upshift-driven improvement of conduction band alignment between the absorber and ETL. EQE results (Fig. S3(a)) reveal higher EQE for KCl-13 cells in the blue spectrum range than that of the KCl-0 cell, which implies better charge collection of the KCl-13 cell through the perovskite-absorber/ETL junction and supports the upshift of CBM for the KCl-13 absorber. The decrease in the band gap is also confirmed by the band gaps extracted from EQE (see the inset of Fig. S3(a) and Fig. S3(b)), where KCl-13 stands out with a slightly decreased band gap. Fig. 5 (panels c–f) shows the statistical data of all the devices. As seen, the FF and V_{oc} are undoubtedly improved via KCl treatment, leading to the

enhanced PCE. The highest PCE was found for the KCl-13 cell, showing 18.54 % (18.13 %) with an FF = 76.06 (74.24 %), V_{oc} = 1.10 V (1.09 V), J_{sc} = 22.16 mA/cm² (22.42 mA/cm²) and reverse (forward) sweeping (Tables S1–S4).

FF and V_{oc} are mainly affected by defects in the bulk absorber or at the interface of the absorber and ETL, which act as charge recombination centers. The defect level and defect density of the perovskite absorber were directly probed via the AS measurements.^{34,35} Fig. 6 (panels a–d) illustrates the AS results for KCl-0 and KCl-13 solar cells. The AS measurement was performed at the 300–180 K temperature range. The deep defect energy level of the perovskite is due to the iodine interstitial (Ii), and the energy level of Ii can be varied by composition and crystallinity of perovskite absorber.^{36,37} Fig. 6 (panels c–d) shows that defect energy level is decreased from 317 meV (KCl-0 cell) to 205 meV (KCl-13 cell) together with a decrease in defect density from 5.6×10^{14} cm⁻³ (KCl-0 cell) to 3.7×10^{14} cm⁻³ (KCl-13 cell). To derive the defect level of the Arrhenius plot, we used the graph of $-\omega dC/d\omega$ vs. ω , as shown in Fig. S4. The reduced defect level is attributed to passivation by K⁺ incorporation into the perovskite absorber. Additionally, the effect of the defect level change by K⁺ diffusion was checked via EIS measurements. Fig. 6(d) presents the EIS results, where R_s = 86.99 Ω and 81.86 Ω for KCl-0 and KCl-13 solar cells, respectively. Note that R_s is regarded as the FTO resistance and is not markedly different between the two cells. Two arcs, large arcs at low frequencies and small arcs at high frequencies, were observed, and they were fitted with an equivalent circuit, as shown in the inset of Fig. 6(e). The large arc is related to recombination resistance (R_{rec}) stemming from charge recombination at the perovskite or perovskite/ETL interface. Thus, a larger R_{rec} implying a longer recombination time is desirable for a higher PCE. The R_{rec} of the KCl-13 cell was calculated to be 4696 Ω , which is much higher than that of the KCl-0 cell (1182 Ω). The increased R_{rec} is ascribed to the defect passivation effect of K⁺ doping, as discussed in the AS result. The small arc is generated from the selective-contact resistance (R_{sc}) of the ETL or HTL.³⁸ R_{sc} is measured to be 196 Ω and 328 Ω for KCl-13 and KCl-0 cells, respectively. The driver of the decreased R_{sc} can be associated with the better conduction band alignment between the absorber and ETL resulting from K⁺ doping.

Considering series resistance (R_{series}) as the sum of R_s and R_{sc} ,³⁸ it is found to decrease in KCl-13 cells. The reduced R_{series} contributes to the improvement of FF and, consequently, the PCE for the KCl-treated devices.

4. Conclusions

We fabricated perovskite solar cells with SnO₂ ETL and KCl-treated SnO₂ ETL and studied the effects of KCl treatment. SIMS depth profiles revealed that K⁺ and Cl⁻ diffused into the perovskite absorber from the surface of the KCl-treated SnO₂. We found that the diffused K⁺ reduced the band gap alongside with the upshift of CBM, which has a beneficial effect on electron transport between the perovskite absorber and ETL. Moreover, the AS measurements indicated that the defect energy level and defect density of the perovskite absorber was reduced by the diffused K⁺, which is a direct evidence of the passivation effect of K⁺ diffusion. Hysteresis in the J-V curve is diminished by the improved conduction band alignment and the passivated interface at perovskite/ETL, and V_{oc} and FF are increased by the passivated perovskite and interface of perovskite/ETL, which all contribute to the enhancement of the PCE of the perovskite solar cell.

Acknowledgements

This work was supported by Incheon National University Research Grant in 2019. The work at the National Renewable Energy Laboratory was supported by the U.S. Department of Energy under Contract No. DE-AC36-08GO28308 with Alliance for Sustainable Energy, Limited Liability Company (LLC), the Manager and Operator of the National Renewable Energy Laboratory.

References

1. NREL Best Research-Cell Efficiency Chart, National Renewable Energy Laboratory, <https://www.nrel.gov/pv/cell-efficiency.html>, accessed May, 2021.
2. Yang, D.; Yang, R.; Zhang, J.; Yang, Z.; Liu, S. F.; Li, C. High efficiency flexible perovskite solar cells using superior low temperature TiO₂. *Energy Environ. Sci.* **2015**, *8*, 3208–3214.
3. Yang, D.; Zhou, X.; Yang, R.; Yang, Z.; Yu, W.; Wang, X.; Li, C.; Liu, S.; Chang, R. P. H. Surface optimization to eliminate hysteresis for record efficiency planar perovskite solar cells. *Energy Environ. Sci.*, **2016**, *9*, 3071–3078.
4. Jung, E. H.; Jeon, N. J.; Park, E. Y.; Moon, C. S.; Shin, T. J.; Yang, T.-Y.; Noh, J. H.; Seo, J. Efficient, stable and scalable perovskite solar cells using poly(3-hexylthiophene). *Nature*, **2019**, *567*, 511–515.
5. Jiang, Q.; Zhao, Y.; Zhang, X.; Yang, X.; Chen, Y.; Chu, Z.; Ye, Q.; Li, X.; Yin, Z.; You, J. Surface passivation of perovskite film for efficient solar cells. *Nat. Photonics*, **2019**, *13*, 460–466.
6. Dong, Q.; Shi, Y.; Zhang, C.; Wu, Y.; Wang, L. Energetically favored formation of SnO₂ nanocrystals as electron transfer layer in perovskite solar cells with high efficiency exceeding 19%. *Nano Energy*, **2017**, *40*, 336–344.
7. Ke, W.; Fang, G.; Liu, Q.; Xiong, L.; Qin, P.; Tao, H.; Wang, J.; Lei, H.; Li, B.; Yang, G.; Yan, Y. Low-Temperature Solution-Processed Tin Oxide as an Alternative Electron Transporting Layer for Efficient Perovskite Solar Cells. *J. Am. Chem. Soc.*, **2015**, *137* (21), 6730–6733.
8. Ke, W.; Xiao, C.; Wang, C.; Saparov, B.; Duan, H.-S.; Zhao, D.; Xiao, Z.; Schulz, P.; Harvey, S. P.; Liao, W.; Meng, W.; Yu, Y.; Cimaroli, A. J.; Jiang, C.-S.; Zhu, K.; Al-Jassim, M.; Fang, G.; Mitzi, D. B.; Yan, Y. Employing Lead Thiocyanate Additive to Reduce the Hysteresis and Boost the Fill Factor of Planar Perovskite Solar Cells. *Adv. Mater.*, **2016**, *28* (26), 5214-5221.
9. Anaraki, E. H.; Kermanpur, A.; Steier, L.; Domanski, K.; Matsui, T.; Tress, W.; Saliba,

- M.; Abate, A.; Grätzel, M.; Hagfeldt, A.; Correa-Baena, J.-P. Highly efficient and stable planar perovskite solar cells by solution-processed tin oxide. *Energy Environ. Sci.*, **2016**, *9*, 3128–3134.
10. Baena, J. P. C.; Steier, L.; Tress, W.; Saliba, M.; Neutzner, S.; Matsui, T.; Giordano, F.; Jacobsson, T. J.; Kandada, A. R. S.; Zakeeruddin, S. M.; Petrozza, A.; Abate, A.; Nazeeruddin, M. K.; Grätzel, M.; Hagfeldt, A. Highly efficient planar perovskite solar cells through band alignment engineering. *Energy Environ. Sci.*, **2015**, *8*, 2928–2934.
 11. Seo, J.-Y.; Matsui, T.; Luo, J.; Correa-Baena, J.-P.; Giordano, F.; Saliba, M.; Schenk, K.; Ummadisingu, A.; Domanski, K.; Hadadian, M.; Hagfeldt, A.; Zakeeruddin, S. M.; Steiner, U.; Grätzel, M.; Abate, A. Ionic Liquid Control Crystal Growth to Enhance Planar Perovskite Solar Cells Efficiency. *Adv. Energy Mater.*, **2016**, *6* (20), 1600767.
 12. Bu, T.; Li, J.; Zheng, F.; Chen, W.; Wen, X.; Ku, Z.; Peng, Y.; Zhong, J.; Cheng, Y.-B.; Huang, F. Universal passivation strategy to slot-die printed SnO₂ for hysteresis-free efficient flexible perovskite solar module. *Nat Commun.*, **2018**, *9*, 4609.
 13. Qiu, L.; Liu, Z.; Ono, L. K.; Jiang, Y.; Son, D.-Y.; Hawash, Z.; He, S.; Qi, Y. Scalable Fabrication of Stable High Efficiency Perovskite Solar Cells and Modules Utilizing Room Temperature Sputtered SnO₂ Electron Transport Layer. *Adv. Funct. Mater.*, **2019**, *29* (47), 1806779.
 14. Jiang, Q.; Zhang, L.; Wang, H.; Yang, X.; Meng, J.; Liu, H.; Yin, Z.; Wu, J.; Zhang, X.; You, J. Enhanced electron extraction using SnO₂ for high-efficiency planar-structure HC(NH₂)₂PbI₃-based perovskite solar cells. *Nat. Energy*, **2016**, *2*, 16177.
 15. Rao, H.-S.; Chen, B.-X.; Li, W.-G.; Xu, Y.-F.; Chen, H.-Y.; Kuang, D.-B.; Su, C.-Y. Improving the Extraction of Photogenerated Electrons with SnO₂ Nanocolloids for Efficient Planar Perovskite Solar Cells. *Adv. Funct. Mater.*, **2015**, *25* (46), 7200–7207.
 16. Liu, Q.; Qin, M.-C.; Ke, W.-J.; Zheng, X.-L.; Chen, Z.; Qin, P.-L.; Xiong, L.-B.; Lei, H.-W.; Wan, J.-W.; Wen, J.; Yang, G.; Ma, J.-J.; Zhang, Z.-Y.; Fang, G.-J. Enhanced

- Stability of Perovskite Solar Cells with Low-Temperature Hydrothermally Grown SnO₂ Electron Transport Layers. *Adv. Funct. Mater.*, **2016**, 26 (33), 6069–6075.
17. Jia, J.; Qian, C.; Dong, Y.; Li, Y. F.; Wang, H.; Ghossoub, M.; Butler, K. T.; Walsh, A.; Ozin, G. A. Heterogeneous catalytic hydrogenation of CO₂ by metal oxides: defect engineering – perfecting imperfection. *Chem. Soc. Rev.*, **2017**, 46, 4631–4644.
 18. Dong, Q.; Shi, Y.; Zhang, C.; Wu, Y.; Wang, L. Energetically favored formation of SnO₂ nanocrystals as electron transfer layer in perovskite solar cells with high efficiency exceeding 19%. *Nano Energy*, **2017**, 40, 336–344.
 19. Dong, Q.; Li, J.; Shi, Y.; Chen, M.; Ono, L. K.; Zhou, K.; Zhang, C.; Qi, Y.; Zhou, Y.; Padture, N. P.; Wang, L. Improved SnO₂ Electron Transport Layers Solution-Deposited at Near Room Temperature for Rigid or Flexible Perovskite Solar Cells with High Efficiencies. *Adv. Energy Mater.*, **2019**, 9, 1900834.
 20. Liu, K.; Chen, S.; Wu, J.; Zhang, H.; Qin, M.; Lu, X.; Tu, Y.; Meng, Q.; Zhan, X. Fullerene derivative anchored SnO₂ for high-performance perovskite solar cells. *Energy Environ. Sci.*, **2018**, 11, 3463-3471.
 21. Xiong, Q.; Yang, L.; Zhou, Q.; Wu, T.; Mai, C.-L.; Wang, Z.; Wu, S.; Li, X.; Gao, P. NdCl₃ Dose as a Universal Approach for High-Efficiency Perovskite Solar Cells Based on Low-Temperature-Processed SnO_x. *ACS Appl. Mater. Interfaces*, **2020**, 12 (41), 46306-46316.
 22. Wang, C.; Zhao, D.; Grice, C. R.; Liao, W.; Yu, Y.; Cimaroli, A.; Shrestha, N.; Roland, P. J.; Chen, J.; Yu, Z.; Liu, P.; Cheng, N.; Ellingson, R. J.; Zhao, X.; Yan, Y. Low-temperature plasma-enhanced atomic layer deposition of tin oxide electron selective layers for highly efficient planar perovskite solar cells. *J. Mater. Chem. A*, **2016**, 4, 12080-12087.
 23. Tao, C.; Neutzner, S.; Colella, L.; Marras, S.; Kandada, A. R. S.; Gandini, M.; Bastiani, M. De; Pace, G.; Manna, L.; Caironi, M.; Bertarelli, C.; Petrozza, A. 17.6% stabilized efficiency in low-temperature processed planar perovskite solar cells. *Energy Environ. Sci.* **2015**, 8, 2365-2370.

24. Yang, D.; Yang, R.; Wang, K.; Wu, C.; Zhu, X.; Feng, J.; Ren, X.; Fang, G.; Priya, S.; Liu, S. F. High efficiency planar-type perovskite solar cells with negligible hysteresis using EDTA-complexed SnO₂. *Nat. Commun.*, **2018**, 9, 3239.
25. Jung, E. H.; Chen, B.; Bertens, K.; Vafaie, M.; Teale, S.; Proppe, A.; Hou, Y.; Zhu, T.; Zheng, C.; Sargent, E. H. Bifunctional Surface Engineering on SnO₂ Reduces Energy Loss in Perovskite Solar Cells. *ACS Energy Lett.*, **2020**, 5, 2796-2801.
26. Liu, X.; Zhang, Y.; Shi, L.; Liu, Z.; Huang, J.; Yun, J. S.; Zeng, Y.; Pu, A.; Sun, K.; Hameiri, Z.; Stride, J. A.; Seidel, J.; Green, M. A.; Hao, X. Exploring Inorganic Binary Alkaline Halide to Passivate Defects in Low-Temperature-Processed Planar-Structure Hybrid Perovskite Solar Cells. *Adv. Energy Mater.*, **2018**, 8 (20), 1800138.
27. Zhu, P.; Gu, S.; Luo, X.; Gao, Y.; Li, S.; Zhu, J.; Tan, H. Simultaneous Contact and Grain-Boundary Passivation in Planar Perovskite Solar Cells Using SnO₂-KCl Composite Electron Transport Layer. *Adv. Energy Mater.*, **2020**, 10 (3), 1903083.
28. Wang, P.; Wang, J.; Zhang, X.; Wang, H.; Cui, X.; Yuan, S.; Lu, H.; Tu, L.; Zhan, Y.; Zheng, L. Boosting the performance of perovskite solar cells through a novel active passivation method. *J. Mater. Chem. A*, **2018**, 6, 15853-15858.
29. Dagar, J.; Hirslandt, K.; Merdasa, A.; Czudek, A.; Munir, R.; Zu, F.; Koch, N.; Dittrich, T.; Unger, E. L. Alkali Salts as Interface Modifiers in n-i-p Hybrid Perovskite Solar Cells. *Sol. RRL*, **2019**, 3 (9), 1900088.
30. Zhu, N.; Qi, X.; Zhang, Y.; Liu, G.; Wu, C.; Wang, D.; Guo, X.; Luo, W.; Li, X.; Hu, H.; Chen, Z.; Xiao, L.; Qu, B. High Efficiency (18.53%) of Flexible Perovskite Solar Cells via the Insertion of Potassium Chloride between SnO₂ and CH₃NH₃PbI₃ Layers. *ACS Appl. Energy Mater.*, **2019**, 2 (5), 3676–3682.
31. Tang, Z.; Bessho, T.; Awai, F.; Kinoshita, T.; Maitani, M. M.; Jono, R.; Murakami, T. N.; Wang, H.; Kubo, T.; Uchida, S.; Segawa, H. Hysteresis-free perovskite solar cells made of potassium-doped organometal halide perovskite. *Sci. Rep.*, **2017**, 7, 12183.
32. Kang, D.-H.; Park, N.-G. On the Current–Voltage Hysteresis in Perovskite Solar Cells: Dependence on Perovskite Composition and Methods to Remove Hysteresis. *Adv.*

Mater., **2019**, 31 (34), 1805214.

33. Lee, J.-W.; Dai, Z.; Lee, C.; Lee, H. M.; Han, T.-H.; Marco, N. De; Lin, O.; Choi, C. S.; Dunn, B.; Koh, J.; Carlo, D. Di; Ko, J. H.; Maynard, H. D.; Yang, Y. Tuning Molecular Interactions for Highly Reproducible and Efficient Formamidinium Perovskite Solar Cells via Adduct Approach. *J. Am. Chem. Soc.*, **2018**, 140, 6317-6324.
34. Duan, H.-S.; Zhou, H.; Chen, Q.; Sun, P.; Luo, S.; Song, T.-B.; Bob, B.; Yang, Y. The identification and characterization of defect states in hybrid organic–inorganic perovskite photovoltaics. *Phys. Chem. Chem. Phys.*, **2015**, 17, 112-116.
35. Heo, J. H.; Song, D. H.; Han, H. J.; Kim, S. Y.; Kim, J. H.; Kim, D.; Shin, H. W.; Ahn, T. K.; Wolf, C.; Lee, T.-W.; Im, S.-H. Planar CH₃NH₃PbI₃ Perovskite Solar Cells with Constant 17.2% Average Power Conversion Efficiency Irrespective of the Scan Rate. *Adv. Mater.*, **2015**, 27 (22), 3424-3430.
36. Du, M.-H. Density Functional Calculations of Native Defects in CH₃NH₃PbI₃: Effects of Spin–Orbit Coupling and Self-Interaction Error. *J. Phys. Chem. Lett.*, **2015**, 6 (8), 1461–1466.
37. Chen, Y.; Li, N.; Wang, L.; Li, L.; Xu, Z.; Jiao, H.; Liu, P.; Zhu, C.; Zai, H.; Sun, M.; Zou, W.; Zhang, S.; Xing, G.; Liu, X.; Wang, J.; Li, D.; Huang, B.; Chen, Q.; Zhou, H. Impacts of alkaline on the defects property and crystallization kinetics in perovskite solar cells. *Nat. Commun.*, **2019**, 10, 1112.
38. Juarez-Perez, E. J.; Wußler, M.; Fabregat-Santiago, F.; Lakus-Wollny, K.; Mankel, E.; Mayer, T.; Jaegermann, W.; Mora-Sero, I. Role of the Selective Contacts in the Performance of Lead Halide Perovskite Solar Cells. *J. Phys. Chem. Lett.*, **2014**, 5 (4), 680-685.

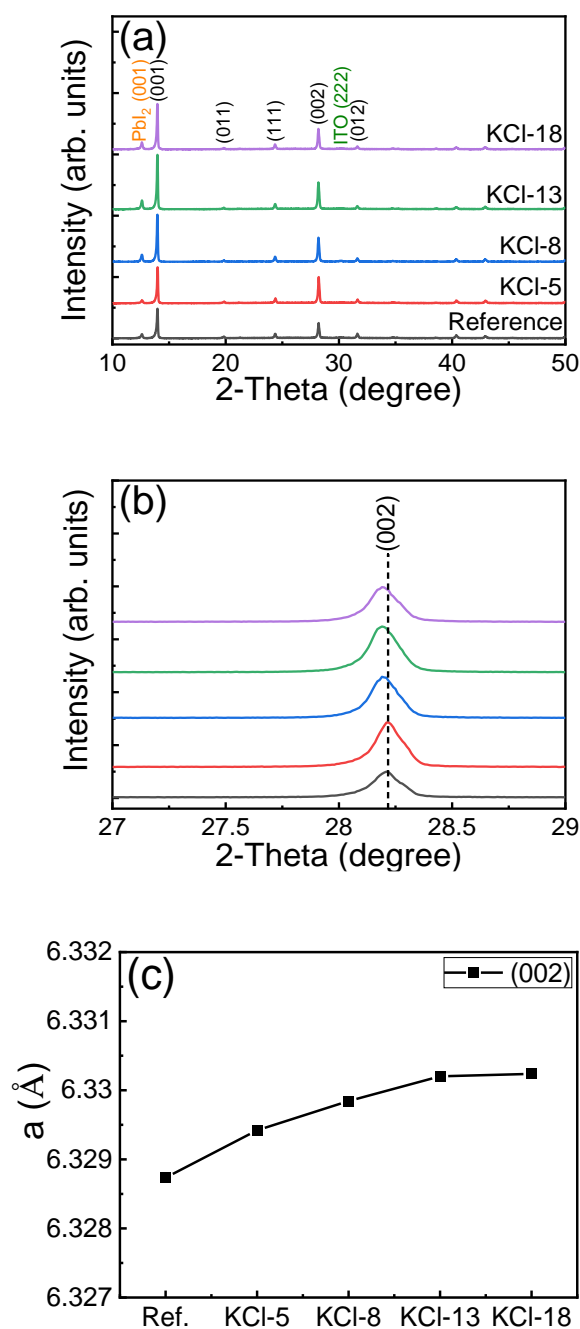


Figure 1. (a) XRD patterns and (b) the magnified (002) peaks of $(\text{FAPbI}_3)_{0.92}(\text{MAPbBr}_3)_{0.08}$ perovskite thin films deposited on SnO_2 without (reference) and with KCl treatment (5–18 mg/mL). (c) Extracted lattice parameter from the corresponding films shown in (a). The lattice parameter is larger with increasing KCl concentration.

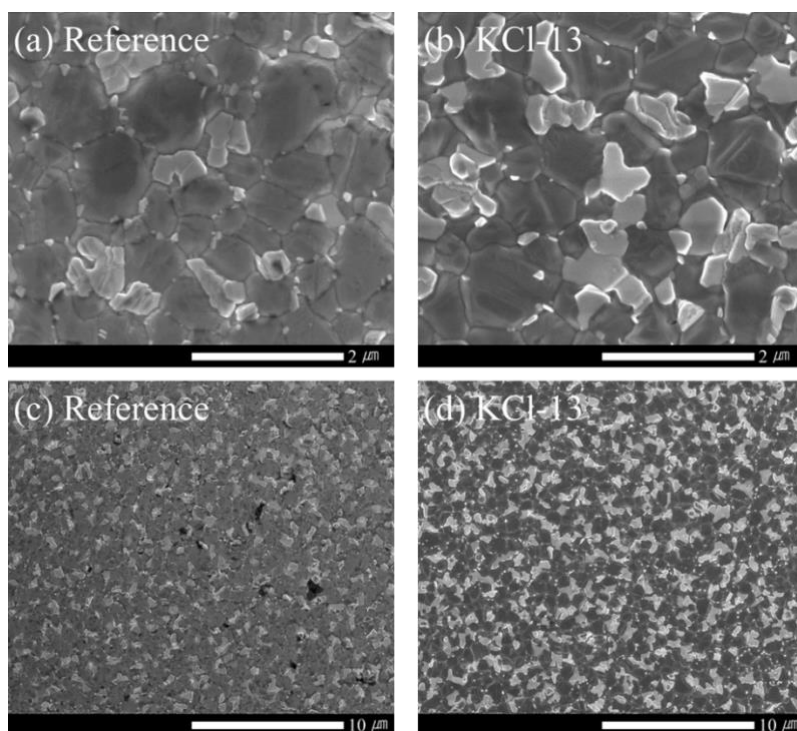


Figure 2. Surface FE-SEM images of $(\text{FAPbI}_3)_{0.92}(\text{MAPbBr}_3)_{0.08}$ perovskite films on SnO_2 without (a, c) and with KCl (13 mg/mL) treatment (b, d) with high (a,b) and low (c,d) magnifications.

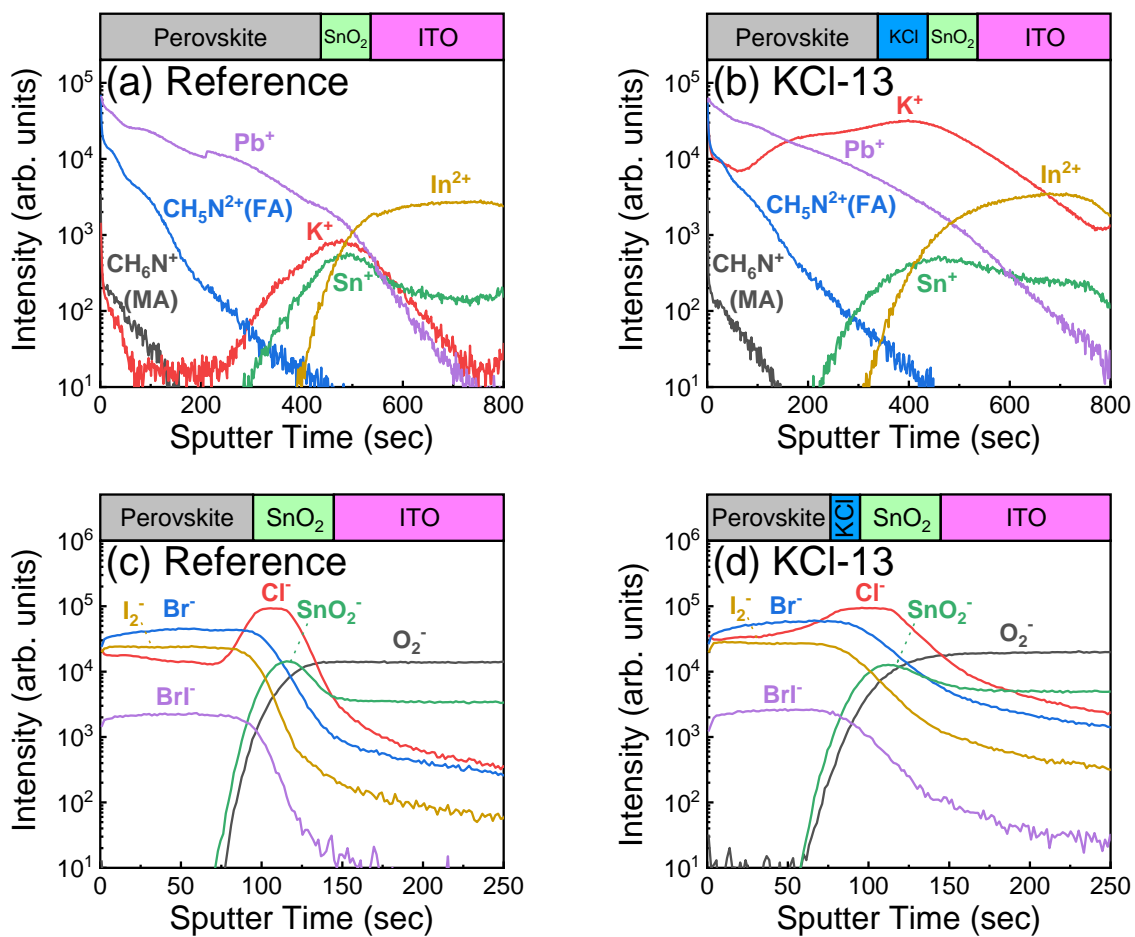


Figure 3. Secondary ion-mass spectroscopy (SIMS) results of $(\text{FAPbI}_3)_{0.92}(\text{MAPbBr}_3)_{0.08}$ perovskite thin films on SnO_2 without (a, c) and with KCl (13 mg/ml) treatment (b, d), where (a, b) are for cation elements and (c, d) are for anion elements distributions, respectively.

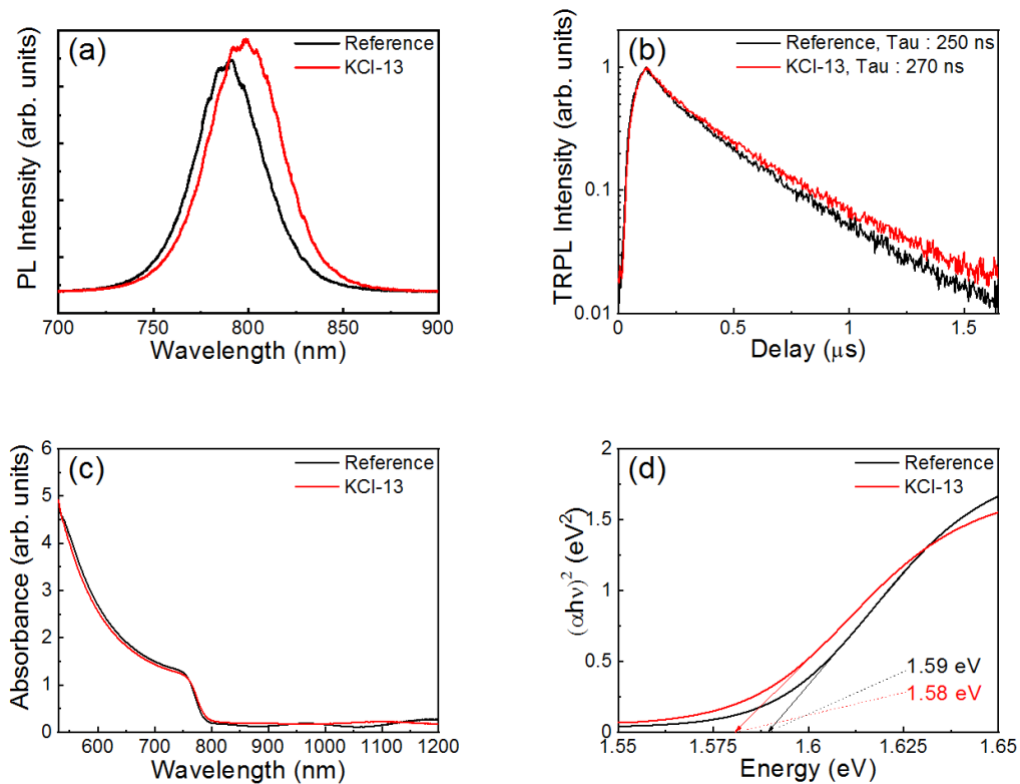


Figure 4. (a) Steady-state PL, (b) TRPL, (c) UV-vis absorption, and (d) the corresponding Tauc analysis for $(\text{FAPbI}_3)_{0.92}(\text{MAPbBr}_3)_{0.08}$ perovskite films on SnO_2 without (reference) and with KCl (13 mg/mL) treatment (KCl-13).

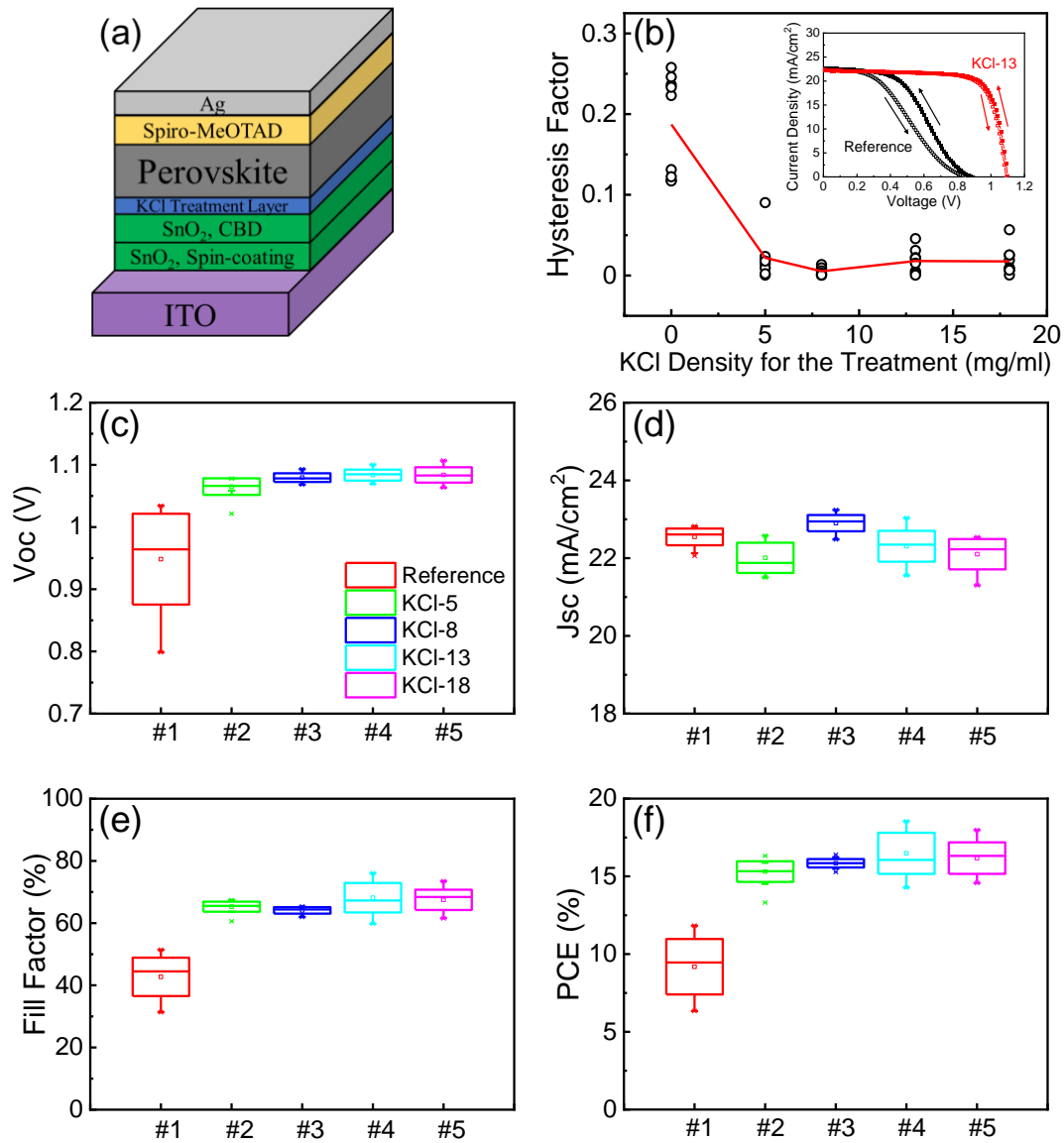


Figure 5. (a) Schematic of fabricated perovskite solar cell. (b) J-V hysteresis factor for fabricated solar cells. Statistical comparison of V_{oc} (c), J_{sc} (d), fill factor (e), and PCE (f) for perovskite solar cells prepared without and with KCl treatment.

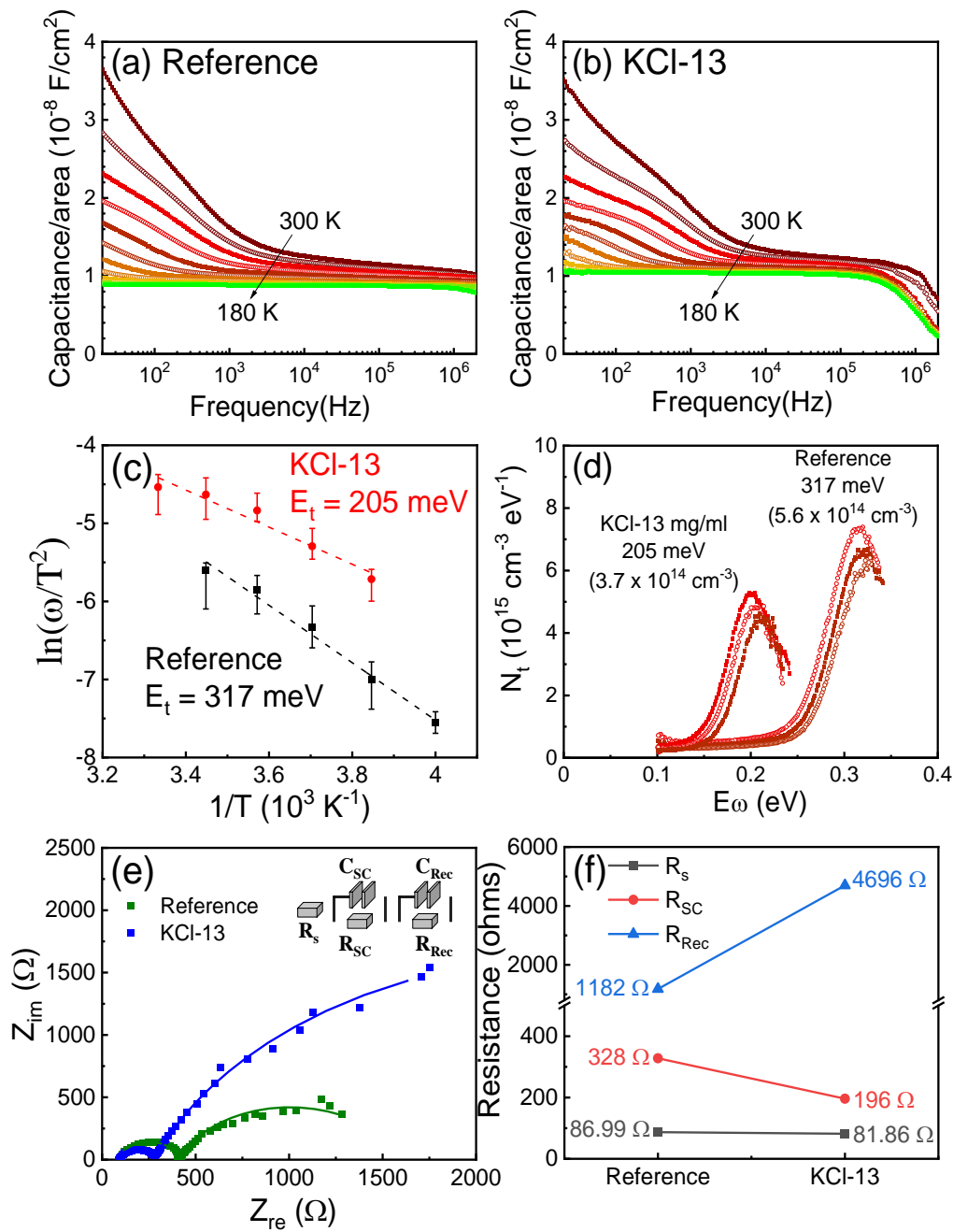


Figure 6. Admittance spectroscopy results of perovskite solar cells prepared without (reference; a) and with KCl (13 mg/mL) treatment (KCl-13; b). Comparison of extracted Arrhenius plots for trap energy levels (c), defect density of states (d), Nyquist plots (e), and the corresponding derived resistances of R_s , R_{SC} and R_{Rec} (f).